

# Role of the Mouse *ank* Gene in Control of Tissue Calcification and Arthritis

Andrew M. Ho,<sup>1\*</sup> Michelle D. Johnson,<sup>1\*</sup> David M. Kingsley<sup>1,2†</sup>

Mutation at the mouse *progressive ankylosis* (*ank*) locus causes a generalized, progressive form of arthritis accompanied by mineral deposition, formation of bony outgrowths, and joint destruction. Here, we show that the *ank* locus encodes a multipass transmembrane protein (ANK) that is expressed in joints and other tissues and controls pyrophosphate levels in cultured cells. A highly conserved gene is present in humans and other vertebrates. These results identify ANK-mediated control of pyrophosphate levels as a possible mechanism regulating tissue calcification and susceptibility to arthritis in higher animals.

Arthritis is one of the most common human health afflictions, affecting 50% of people over 65 and accounting for \$100 billion in medical costs and lost productivity each year (1). As the population ages, the health and economic tolls of arthritis are predicted to increase dramatically in the future (2). Despite the tremendous individual and social impact of arthritis, its underlying causes are not well understood. Twin studies suggest that genetic factors account for half to two-thirds of human arthritis cases, including the most common types such as osteoarthritis, rheumatoid arthritis, and ankylosing spondylitis (3–5). Several genetic susceptibility factors have been identified, including specific major histocompatibility complex (MHC) alleles and rare mutations in cartilage matrix genes (6).

Mice carrying the *ank* mutation have been studied as a model of arthritis (7–12). The autosomal recessive *ank* mutation causes an abnormal, flat-footed gait in young mice due to decreased mobility of ankle and toe joints. Loss of joint mobility becomes more severe with age and spreads to most joints throughout the limbs and vertebral column, leading to complete rigidity and death around 6 months of age (7).

Hydroxyapatite crystals develop in articular surfaces and synovial fluid of *ank* mice, accompanied by joint space narrowing, cartilage erosion, and formation of bony outgrowths or osteophytes that cause fusion (ankylosis) and joint immobility (7, 8, 10, 11). Although the distribution and severity of phe-

notypes do not precisely mimic any single form of human arthritis, many of the pathological features in *ank* mice are reminiscent of cardinal features in several important arthritic diseases, including ectopic calcification seen in mineral deposition disease, cartilage erosion and osteophyte formation seen in osteoarthritis, and vertebral fusion seen in ankylosing spondylitis (7, 8, 10, 11).

Despite extensive studies over the last 20 years, the genetic defect in *ank* mice has remained elusive. Here, we identify the *ank* gene product, study its functional properties, and propose a model that may explain its pathogenic role in arthritis and mineral formation.

**Genetic and physical mapping.** Previous studies mapped the *ank* locus to proximal mouse chromosome 15 (7). To narrow the location of the gene, we generated 923 F<sub>2</sub> *ank/ank* mice from a cross with *Mus musculus castaneus* (13). Linkage analysis identified two microsatellite markers that failed to recombine with the *ank* trait in the high-resolution genetic cross, placing the markers at less than 0.06 centimorgan (cM) from the *ank* mutation (Fig. 1).

The *D15Mit20* marker was used as a molecular entry point to build a physical map of the *ank* region (14). Multiple rounds of chromosome walking led to the isolation of a ~400-kb interval in bacterial artificial chromosome (BAC) clones (Fig. 1). End probes from BACs A and H recognized three and two recombination events, respectively, that mapped on opposite sides of *ank* in the high-resolution mapping cross (Fig. 1), showing that the *ank* mutation must lie in the cloned region.

**In vivo complementation and BAC transgenic mice.** To narrow the candidate interval, we tested whether individual BAC clones could rescue *ank* mutant phenotypes in transgenic mice (15). Control *ank/ank* mutants were unable to grasp a wire cage top at

weaning age due to stiffness in the digits. Histological sections of the joints in these mice showed obvious arthritic features like joint space narrowing, cartilage erosion, accumulation of debris in the joint space, and ectopic calcification in and around the affected joints (Fig. 2, D to F). In contrast, *ank/ank* mice carrying BAC C showed normal digit mobility and normal joint morphology (Fig. 2, G to I). Functional and histological rescue were seen in three independent BAC C transgenic lines evaluated at both 5 weeks and 3 months of age. These data suggest that the *ank* mutant phenotypes arise from decreased function of a gene contained in BAC C.

**Identification of the *ank* mutation.** To identify candidate genes in the critical region, we used shotgun sequencing to generate ~450 kb of random sequence from BAC C (16). BLAST searches identified portions of 11 candidate groups in the nonredundant and expressed sequence tag (EST) databases of GenBank. None of the candidate genes showed any obvious relation to arthritis or displayed any differences in wild-type and

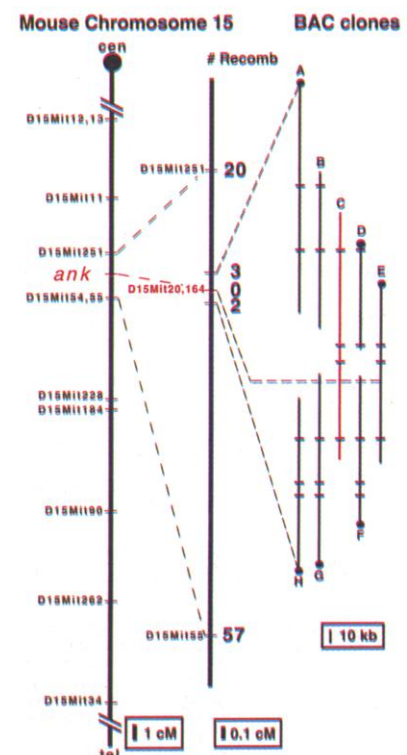


**Fig. 1.** Genetic and physical map of the *ank* locus. High-resolution genetic mapping localizes the *ank* mutation to a region between *D15Mit251* and *D15Mit55*. The nonrecombinant marker *D15Mit20* was used to initiate a chromosome walk in the *ank* region. Black bars indicate *Bss*H II sites in overlapping BAC clones. End probes (black circles) from BACs A and H map to opposite sides of *ank* (number of recombinants shown), and define an interval of ~400 kb that must contain the mutation. The rescuing BAC C is highlighted in red and further narrows the critical region to ~190 kb.

<sup>1</sup>Department of Developmental Biology and <sup>2</sup>Howard Hughes Medical Institute, Beckman Center B300, Stanford University School of Medicine, Stanford, CA 94305-5327, USA.

\*These authors contributed equally to this work.

†To whom correspondence should be addressed. E-mail: kingsley@cmgm.stanford.edu

mutant samples by Northern or Southern blot analysis. However, further sequencing studies (16) identified a single nucleotide G to T substitution in one of the candidate genes in *ank* mutant mice (Fig. 3B). This base change creates a nonsense mutation in the corresponding open reading frame (ORF) and is predicted to destroy a *Hinf* I restriction site in genomic DNA. Amplification of the corresponding region from wild-type and mutant mice followed

by *Hinf* I digestion confirmed the sequence change in *ank* mutant mice (Fig. 3C) (16). This sequence change was not found in 17 wild-type inbred strains surveyed (16), indicating that the G to T substitution is not a common strain polymorphism. Most importantly, the nucleotide change was not present in the JGBF strain in which the *ank* mutation arose (7), strongly suggesting that the single base substitution is the *ank* mutation.

**Features of the predicted ANK protein.**

The nucleotide sequence of this gene matches two split GenBank entries for an unpublished gene previously identified in mitogen-stimulated murine prostate carcinoma cells (17). We refer to the gene as *ank*, and its corresponding protein as ANK, in accordance with the name of the original mouse locus. The *ank* gene is predicted to encode a 492 amino acid protein (Fig. 3A), with an expected molecular mass of 54.3 kD and an isoelectric point of 8.01. The predicted protein contains three potential N-linked glycosylation sites and multiple putative phosphorylation sites. A hydrophathy analysis with the Kyte-Doolittle algorithm (18) revealed 9 to 12 hydrophobic stretches (Fig. 4A). Most are ~20 residues long, as would be expected for membrane-spanning regions in an integral multipass transmembrane protein. Further analysis with sequence homology and motif scanning algorithms did not identify any significant functional domains in ANK, suggesting that ANK is a previously unknown protein.

**Protein expression and subcellular localization.** To characterize the ANK protein, we generated an expression construct (pCMV-ANK) by cloning the *ank* ORF into a mammalian expression vector (pCMV) (19). This construct was transfected into COS-7 monkey kidney cells (20), and protein extracts were collected and analyzed by Western blotting with rabbit polyclonal antibodies raised against various peptide epitopes in ANK (Fig. 4A) (19). These antibodies detected a major protein band of ~50 kD in pCMV-ANK-transfected but not pCMV-transfected cells (21). To determine the subcellular localization of ANK protein, we used

**Fig. 2.** BAC C rescues the *ank* phenotype. (A to C) Hind limb interphalangeal joints from 3-month-old wild-type mice show normal empty joint space flanked by smooth, unmineralized articular cartilage. Joints were stained with alizarin red (A), or sectioned and stained with hematoxylin and eosin (B) or with von Kossa's calcium staining method (C). Scale bars: 250  $\mu$ m in (A) and 50  $\mu$ m in (B). (D to F) Age-matched joints of *ank/ank* mutant mice show joint space narrowing, articular cartilage erosion [asterisks in (E) and (F)], calcified debris on articular cartilage and in joint space [arrowheads in (E) and (F)], and excessive calcification (F). (G to I) Joints of *ank/ank* mutant mice carrying BAC C are indistinguishable from wild-type mice.

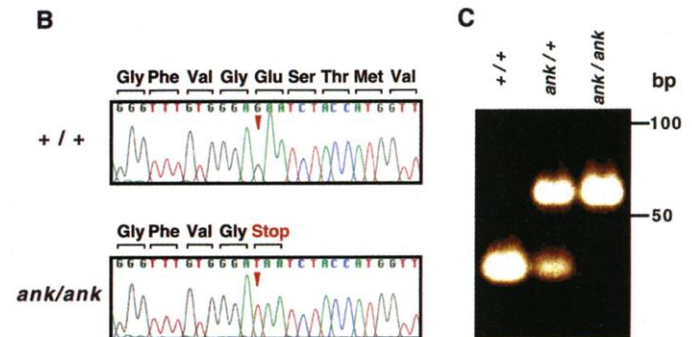
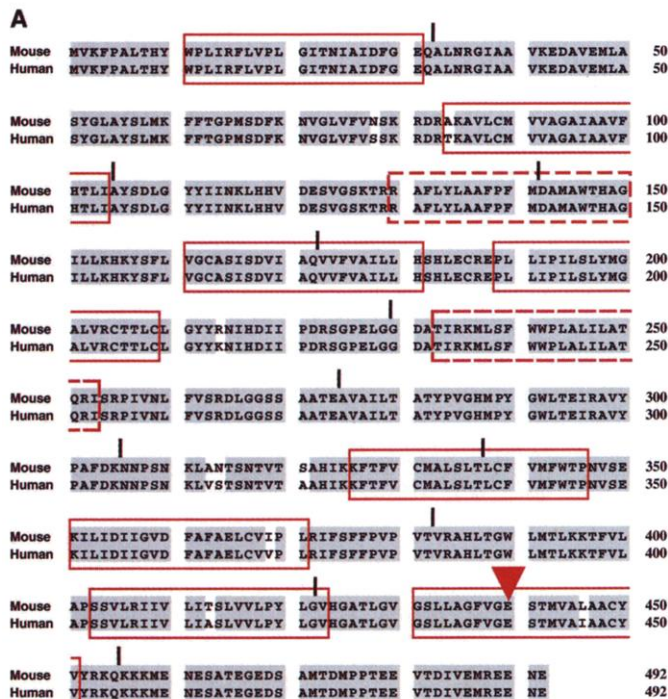
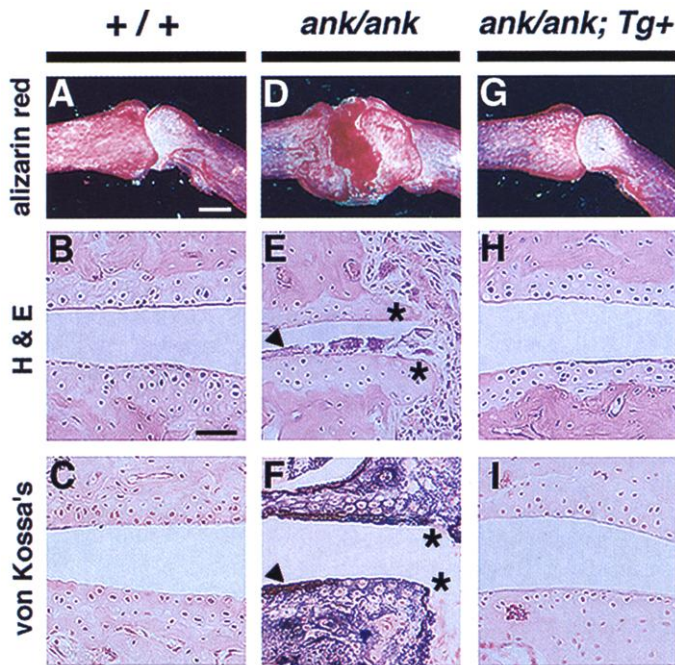


**Fig. 3.** *ank* mutation disrupts a highly conserved hydrophobic protein. (A) Mouse and human ANK proteins are nearly identical. Dashed boxes or solid boxes denote regions predicted by the Kyte-Doolittle algorithm (18) to be either likely or certain transmembrane domains, respectively. Black bars, exon boundaries in the gene; red arrowhead, position of *ank* mutation. Mouse and human sequences have been deposited in GenBank (accession numbers AF274752 and AF274753, respectively). (B) Sequence traces showing a G to T substitution in *ank* mutant mice (small arrowheads in chromatogram), changing the codon for Glu<sup>440</sup> to a stop codon. (C) Confirmation of sequence change in genomic DNA. A 58-bp region amplified around the site of the *ank* mutation is cleaved by *Hinf* I in wild-type mice, partially cleaved in *ank/+* heterozygous mice, and not cleaved in *ank/ank* mice.

the same antibodies for indirect immunofluorescence on transfected cells (19). Cells transfected with pCMV did not show any appreciable signal (21). In contrast, cells transfected with pCMV-ANK exhibited an intense ring of immunoreactivity on the cell surface, suggesting that ANK is a membrane protein. A subset of cells (30 to 50%) also showed weaker immunoreactivity in the cytoplasm in addition to the cell surface ring (21). Similar results were seen with three different antibodies [Ab1 and Ab3 (Fig. 4B) and Ab2 (21)]. The ANK signal was detectable only in permeabilized cells, suggesting that the epitopes recognized by Ab1, Ab2, and Ab3 are likely to be cytoplasmic. Figure 4C shows one possible transmembrane topology that is consistent with the results from sequence prediction and immunofluorescence experiments (22).

**Expression pattern.** Northern blot analysis revealed that the *ank* mRNA is expressed in many tissues in adult mice including heart, brain, liver, spleen, lung, muscle, and kidney (Fig. 5A) (23). Although soft tissue phenotypes have not previously been reported in *ank* mice, we have observed increased calcification in kidneys of adults, consistent with an important role

for the gene in nonskeletal tissues (24). In situ hybridization analysis of developing mouse limbs showed strong *ank* expression in the developing articular cartilage of joints in the shoulder, elbow, wrist, and digits (Fig. 5, B, D, and F) (23), tissues that are severely affected in adult *ank* mutants.

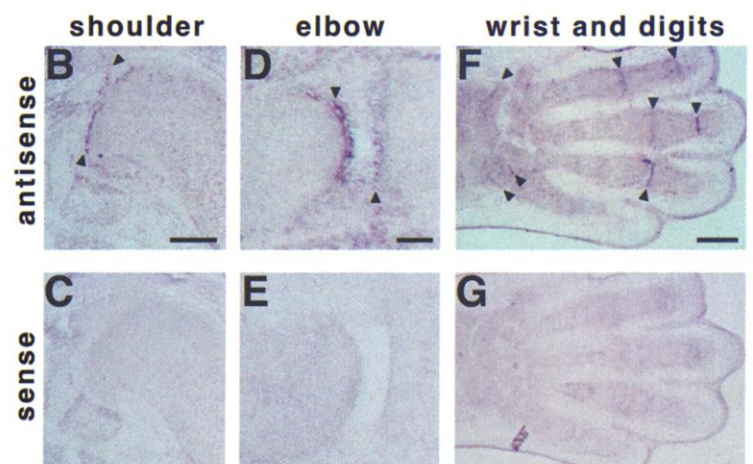
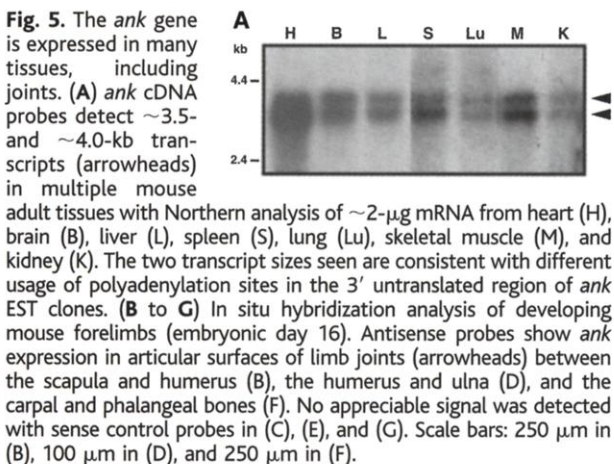
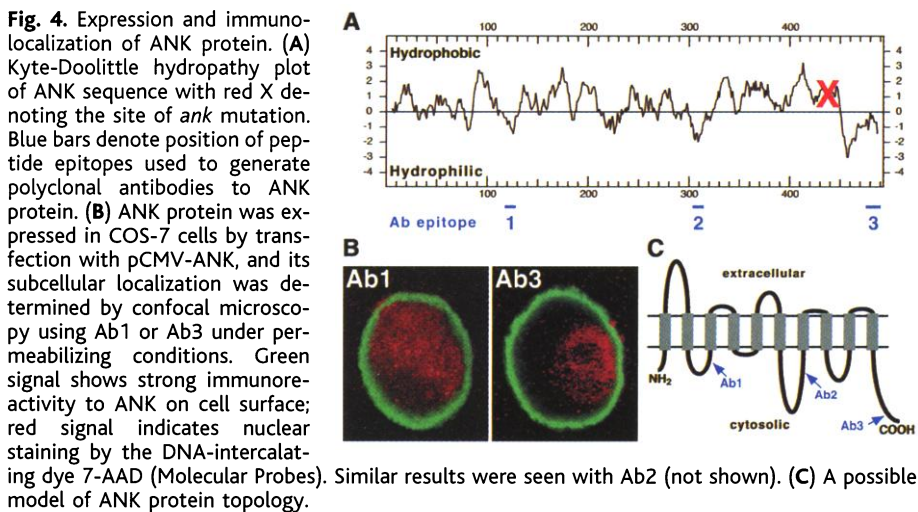
**Cloning of a human ortholog of the *ank* gene.** Database searching with the full-length mouse *ank* sequence identified no clear homologs in the extensive genome sequences available for bacteria, yeast, worms, and flies. In contrast, the primary sequence of the *ank* gene is highly conserved in EST clones from many vertebrates, including zebrafish, rats, mice, cows, and humans. Using the exon/intron structure of the mouse gene and the partial sequence from human EST clones, we amplified and sequenced the complete coding region of human ANK (25). The human ANK protein is nearly identical to mouse ANK over its entire length, with only 9 amino acid substitutions out of 492 amino acids (Fig. 3A). Radiation hybrid mapping shows that the human gene maps to a homologous region on human chromosome 5p, closely linked to *D5S1954* (26). Interestingly, the genetic defects in several human pedigrees with arthri-

tis and chondrocalcinosis map to the same chromosomal region (27–29). Like *ank* mutants, affected family members show precocious calcification, pain, or arthritis in synovial joints. The sequence identity and map location suggest that the function of the *ank* gene may be highly conserved in vertebrates.

**ANK functions in pyrophosphate regulation.** Increased levels of intracellular inorganic pyrophosphate (PP<sub>i</sub>) have previously been reported in cultured skin fibroblasts and lymphoblasts from one of the human families whose genetic defect maps to the chromosome 5p region containing ANK (30). To determine if *ank* mutants have a similar defect in PP<sub>i</sub> metabolism, we established primary skin fibroblast cultures from wild-type and mutant mice (31). Fibroblasts from *ank* mutants displayed about twofold increase in intracellular PP<sub>i</sub> levels (31) over wild-type cells (Fig. 6A) ( $P < 0.01$ ), a change similar to that previously reported for cells from the human patients (30).

PP<sub>i</sub> and its derivatives are potent inhibitors of calcification both in vitro and in vivo (32). PP<sub>i</sub> is present in synovial fluid, plasma, and urine at levels sufficient to block calcification and has been postulated to be a natural inhibitor of hydroxyapatite formation in fluids outside cells (33, 32). To test whether the defect in *ank* mice might also affect extracellular PP<sub>i</sub>, we collected conditioned media from wild-type and mutant fibroblasts and measured their PP<sub>i</sub> levels (31). The *ank* mutation caused a three- to fivefold decrease in extracellular PP<sub>i</sub> levels (Fig. 6A) ( $P < 0.005$ ), in contrast to its stimulatory effect on intracellular PP<sub>i</sub>. Thus, the *ank* gene appears to regulate both intra- and extracellular levels of an important inhibitor of hydroxyapatite crystal formation.

To determine if the cloned *ank* gene could rescue the PP<sub>i</sub> abnormalities in the mutant cells, we transfected wild-type and *ank* mutant fibroblasts with pCMV-ANK and assayed PP<sub>i</sub> levels (34). Both the increase in intracellular PP<sub>i</sub> and the decrease in extracel-



lular  $PP_i$  observed in *ank* mutant cells were abolished when ANK expression was restored in these cells (Fig. 6B), indicating that *ank* is the gene responsible for the mutant phenotypes.

To explore how perturbations in ANK activity change cellular  $PP_i$  levels, we also investigated the effect of high-level ANK expression in COS-7 cells (34). Whereas a loss of ANK function in mutant fibroblasts increased intracellular  $PP_i$  levels and decreased extracellular  $PP_i$  levels, a gain of ANK function in COS-7 cells caused a dramatic drop in intracellular  $PP_i$  to undetectable levels (Fig. 6C) ( $P < 0.001$ ) and a two- to fourfold rise in  $PP_i$  levels in the conditioned medium (Fig. 6C) ( $P < 0.001$ ). In contrast, introduction of the *ank* mutation into the expression construct drastically reduced its effects on  $PP_i$  levels (intracellular pyrophosphate levels of 100%, 0%, and 48% were seen after transfection with control, wild-type, and mutant constructs, respectively).

The opposite effects of ANK on  $PP_i$  levels inside and outside cells could be explained if ANK normally functions in  $PP_i$  transport. To test this model, we examined the effects of probenecid, a weak organic acid that inhibits anion transport (35). Previous studies suggest

that articular chondrocytes have a  $PP_i$ -transport activity that is blocked by 5-mM probenecid (36). When transfected COS-7 cells expressing ANK were treated with 2.5 mM probenecid, the ANK-mediated drop in intracellular  $PP_i$  was completely blocked (Fig. 6D). This suggests that ANK is functioning through a probenecid-sensitive anion transport mechanism, or that probenecid has additional effects on cells that can counteract ANK function.

**Discussion.** We have identified a previously unknown, multiple-pass transmembrane protein as the product of the *ank* locus. The original mouse mutation creates a nonsense codon that truncates the COOH-terminal region of the protein and greatly reduces its activity in vitro. The contrasting effects of the ANK gene product on intracellular and extracellular  $PP_i$  levels are most simply explained if ANK acts as a transmembrane transporter that shuttles  $PP_i$  between intracellular and extracellular compartments (Fig. 7). Because  $PP_i$  is charged and polar, any movement of  $PP_i$  through the cell membrane is likely to involve a specialized channel or transporter. A loss of this transporter function would result in intracellular accumulation and extracellular drop in  $PP_i$ , as observed in

the *ank* mutant cells. In contrast, an increase in transporter activity would lead to an increase in extracellular levels and a drop in intracellular levels, as seen in the transfected COS cell assays. The multipass transmembrane structure of the ANK protein and its sensitivity to the anion transport inhibitor probenecid are also consistent with a direct role in  $PP_i$  transport. It is possible that ANK affects transport or cotransport of other small molecules in addition to  $PP_i$ , or controls intracellular and extracellular  $PP_i$  through independent metabolic effects both inside and outside cells.

How could a defect in  $PP_i$  regulation lead to the dramatic joint calcification and arthritic destruction seen in *ank* mice? Many previous studies have shown that  $PP_i$  is a potent inhibitor of calcification, bone mineralization, and bone resorption in vitro and in vivo (32).  $PP_i$  was purified from urine in a screen for natural agents that inhibit formation of calcium phosphate crystals (32, 33). Addition of  $PP_i$  to organ culture blocks mineralization of growing bone, and injection in vivo blocks ectopic calcification induced by vitamin D (37, 38). Human defects in alkaline phosphatase, an enzyme that degrades  $PP_i$ , lead to an increase in  $PP_i$  levels and a severe block in skeletal mineralization in vivo (39). Conversely, genetic defects in a cell surface ectoenzyme that normally generates extracellular  $PP_i$  from nucleotide triphosphate cause ectopic mineralization of joints and ligaments in the mouse mutant *tiptoe walking* (40)

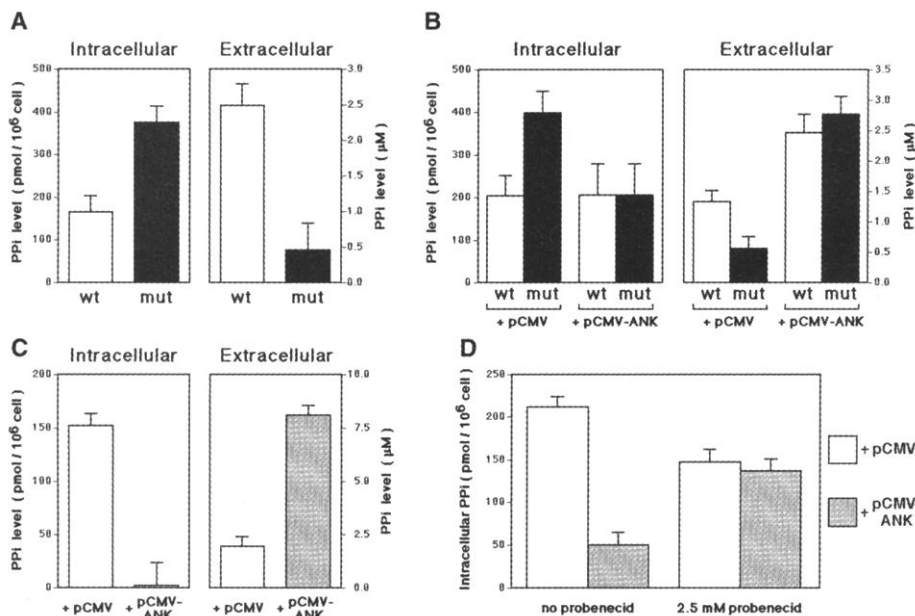


**Fig. 6.** ANK activity controls pyrophosphate levels in cultured cells. (A) Primary skin fibroblasts isolated from adult wild-type (wt) or age- and sex-matched *ank/ank* mutant (mut) mice show striking differences in levels of intracellular and extracellular pyrophosphate ( $PP_i$ ). In this and all other panels, error bars denote standard deviations from quadruplicate pyrophosphate assays conducted on each sample. All results were confirmed in at least three independent experiments. (B) Expression of ANK protein reverses the alterations in  $PP_i$  levels. Wild-type and *ank* mutant fibroblasts were transfected with a control vector (+ pCMV) or the same vector driving expression of ANK (+ pCMV-ANK), and  $PP_i$  levels were measured ~48 hours later. (C) Overexpression of ANK in COS cells causes dramatic drop in intracellular  $PP_i$  and rise in extracellular  $PP_i$  levels. COS-7 cells were transfected with a control vector (+ pCMV) or the ANK expression construct (+ pCMV-ANK).  $PP_i$  levels were determined ~48 hours later. (D) The effect of the ANK gene is blocked by the anion transport inhibitor probenecid. COS-7 cells were transfected with pCMV or pCMV-ANK. After ~30 hours, the media were replaced with control medium or with medium containing 2.5 mM probenecid. Intracellular  $PP_i$  levels were determined 12 hours later.

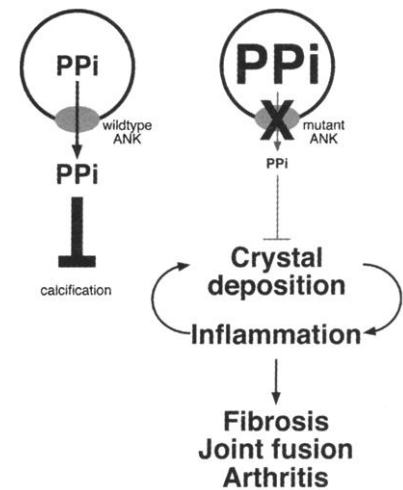


**Fig. 7.** Working model for the role of ANK in tissue calcification and arthritis. Expression of wild-type ANK leads to elaboration of extracellular  $PP_i$ , most likely by a transport mechanism. Local elaboration of  $PP_i$  provides a natural inhibitor of hydroxyapatite deposition, blocking unwanted mineralization in articular cartilage and other tissues. With loss of ANK activity, extracellular  $PP_i$  levels drop, intracellular  $PP_i$  levels rise, and unregulated calcification begins in the joints, triggering a destructive cycle (49) of mineral deposition, inflammation, and osteophyte formation leading to arthritis.

and may be associated with spinal ligament ossification in humans (41).

The ability of  $PP_i$  to inhibit mineral deposition has been widely applied in dentistry to control unwanted mineralization. The active ingredient in most tartar control toothpaste formulations is  $PP_i$ , which inhibits formation of the calcified mineral deposits typically found in tartar (42). The *ank* gene may provide a natural form of tartar control for the synovial joints of vertebrates. Articular cartilage is one of the few locations that normally remains unmineralized in the vertebrate skeleton. The *ank* gene is expressed in developing articular surfaces and may help maintain the unmineralized state by providing a local source of  $PP_i$  to inhibit hydroxyapatite formation. In the absence of normal *ank* activity, mineralization extends unhindered throughout articular cartilage, hydroxyapatite deposits form in synovial fluid, and new bone is deposited in and around joints, showing that the gene is essential for normal joint maintenance.

If  $PP_i$  dysregulation is the underlying cause of *ank* phenotypes, the arthritic defects in *ank* mice should be rescued when normal  $PP_i$  levels are restored. This is difficult to test with  $PP_i$  itself, which is degraded rapidly when administered systemically (32). However, structural analogues of  $PP_i$  have been developed that are more stable in vivo, including bisphosphonates (32) and phosphocitrate. Like  $PP_i$ , phosphocitrate is a potent inhibitor of hydroxyapatite crystal deposition (43). Daily injections of phosphocitrate block mineral deposition, osteophyte formation, and joint immobility defects in *ank* mutants (44), providing additional evidence that ANK controls mineral deposition in vertebrate joints.

Deposition of calcium-containing crystals in joints is common in humans. Up to 5% of the human population shows radiographic evidence of chondrocalcinosis, with the incidence rising to over 40% in the elderly (45, 46). More than 60% of osteoarthritis patients show evidence of calcium pyrophosphate crystals, hydroxyapatite crystals, or both, in synovial fluid (47, 48). A longstanding debate in the rheumatology field has been whether such crystals are a primary cause of arthritis or a secondary consequence of joint damage (45, 49–51). Calcium crystals can stimulate release of proteases and inflammatory cytokines from cultured synovial cells, and direct injection of crystals into joints causes arthritis in experimental animals. Joint damage in turn can also stimulate secondary crystal deposition (45, 49–51). *Progressive ankylosis* and *tiptoe walking* mice provide clear examples of generalized arthritis syndromes that can be traced to primary defects in the control of mineral formation. These mutants strongly suggest that genetic defects in the mechanisms that control  $PP_i$  levels can

be an important primary cause of osteophyte formation and joint destruction in arthritis (Fig. 7).

Several human pedigrees with joint abnormalities have been mapped to the same chromosomal region as human *ANK* (27–29). Affected family members display precocious calcification in and around affected joints and clinical symptoms variously described as chondrocalcinosis, pseudogout, pseudorheumatoid arthritis, or pseudoosteoarthritis. Fibroblasts from patients of one of these families show elevation of intracellular  $PP_i$  (30), an alteration similar to that seen in fibroblasts from *ank* mice. It will be interesting to test whether familial forms of human arthritis linked to chromosome 5p, as well as more common forms of mineral deposition and joint disease seen in the general human population, can be explained by genetic variation in the human *ANK* gene. ANK activity may also be a useful target for the development of new therapies for arthritis and many other human diseases involving abnormal mineral deposition.

#### References and Notes

1. E. Yelin and L. F. Callahan, *Arthritis Rheum.* **38**, 1351 (1995).
2. C. G. Helmick *et al.*, *Arthritis Care Res.* **8**, 203 (1995).
3. T. D. Spector *et al.*, *Br. Med. J.* **312**, 940 (1996).
4. M. A. Brown *et al.*, *Arthritis Rheum.* **40**, 1823 (1997).
5. A. J. MacGregor *et al.*, *Arthritis Rheum.* **43**, 30 (2000).
6. P. Wordsworth, *Br. Med. Bull.* **51**, 249 (1995).
7. H. O. Sweet and M. C. Green, *J. Hered.* **72**, 87 (1981).
8. F. T. Hakim *et al.*, *Arthritis Rheum.* **27**, 1411 (1984).
9. F. T. Hakim, K. S. Brown, J. J. Oppenheim, *Arthritis Rheum.* **29**, 114 (1986).
10. H. W. Sampson and J. S. Davis, *Spine* **13**, 650 (1988).
11. M. L. Mahowald, H. Krug, P. Halverson, *J. Rheumatol.* **16**, 60 (1989).
12. H. E. Krug *et al.*, *J. Rheumatol.* **24**, 115 (1997).
13. The *ank* and *M. castaneus* stocks were obtained from The Jackson Laboratory (Bar Harbor, ME). Phenotypes of 4138  $F_2$  progeny were scored at 5 weeks of age by testing the ability of mice to grip a wire cage grid, and by alizarin red skeletal staining. Sixty affected  $F_2$  mice were initially screened with 11 MapPair microsatellite markers (Research Genetics, Huntsville, AL), and all 923 affected  $F_2$  progeny were subsequently typed with *D15Mit251* and *D15Mit55*. Seventy-seven mice with recombination between these markers were then typed with 26 additional microsatellite markers. *D15Mit20* and *D15Mit164* showed no recombination with the *ank* trait in the high-resolution mapping panel.
14. The CITB Release II library (Research Genetics) was screened with *D15Mit20*. BAC end probes were isolated with bubble polymerase chain reaction (PCR) [J. Riley *et al.*, *Nucleic Acids Res.* **18**, 2887 (1990)] and were used for additional rounds of chromosome mapping. Contigs were assembled by pulsed-field gel mapping and cross-hybridization of BAC end probes. BACs B to H correspond to clones 307D1, 282M13, 456B18, 110PB, 477E24, 284I20, and 144P21, respectively. BAC A corresponds to clone 104F8 (Genome Systems, St. Louis, MO).
15. Circular BAC DNA (0.3 to 1.0 ng/ $\mu$ l) was microinjected into fertilized FVB mouse oocytes at the Stanford Transgenic Research Facility. Founder mice were mated to *ank* mutants, and the *ank*<sup>+/+</sup>, *tg*<sup>+</sup> progeny were intercrossed. The *ank/ank* progeny were identified by homozygosity of alleles at the *D15Mit180* locus, and transgenic carriers were identified by Southern blot analysis with a BAC vector probe. Mouse limbs were partially decalcified for 12 to 24 hours in Calex II (Fisher, Pittsburgh, PA), fixed in 10% formalin, dehydrated in ethanol, cleared in xylene, and embedded in paraffin wax. Adjacent 6- $\mu$ m sections were collected and stained with hematoxylin and eosin or with von Kossa's method.
16. DNA from BAC C was sheared mechanically to 2 to 3 kb and subcloned into the Eco RV site of pBluescript SK(+) (Stratagene, La Jolla, CA) by blunt end ligation. Clones were sequenced with both T3 and T7 primers and the ABI Prism Dye Terminator Kit (PE Applied Biosystems, Foster City, CA). Candidate genes were amplified from total brain RNA of wild-type and mutant mice with gene-specific primers and ThermoScript reverse transcriptase (Gibco-BRL, Grand Island, NY). Initial cDNA products were treated with 2 U ribonuclease H (RNase H) at 37°C (30 min) and amplified with forward and reverse primers. Secondary PCR products were purified on a 1% low-melt agarose gel (FMC Bioproducts, Rockland, ME), extracted with the Ultraclean Gelspin DNA purification kit (Doc Frugal Scientific, San Diego, CA), and sequenced with gene-specific primers. The genomic region surrounding the *ank* mutation was amplified from *ank/ank*, JGBF, 129/J, A/J, AKR/J, Balb/cByJ, BTBR(+T), C3H/HeJ, C57BL/6J, C57BR/cdJ, C57L/J, CAST/Ei, CBA/J, CZECHII/Ei, DBA/2J, FVB/NJ, NZB/BINJ, P/J, and SPRET/Ei strains (DNA Resource, The Jackson Laboratory) with GGCTCCCTCTAGCAGGTT and AGCATGCTGCAAGGGCAACC primers, digested with Hinf I, and analyzed by electrophoresis in a 4% agarose gel.
17. GenBank accession numbers AF001532 and AF001533.
18. M. G. Claros and G. von Heijne, *Comput. Appl. Biosci.* **10**, 685 (1994).
19. Full-length *ank* cDNA was amplified from total brain RNA with forward and reverse primers that flank the *ank* ORF (CGCGGATCCACCATGGTAAATCCCGCGCC, CGCGGATCCATCTACTATTTCTCTCTCATCTCT). Amplified products were digested with Bam HI, subcloned into the Bam HI site of pCDNA3 (Invitrogen, Carlsbad, CA), and sequenced to verify the structure of the insert. Rabbit polyclonal antibodies were generated against keyhole limpet hemocyanin (KLH)-conjugated peptides containing amino acids 118 to 130 (Ab1), 304 to 317 (Ab2), and 477 to 492 (Ab3) of murine ANK by Zymed Laboratories (San Francisco, CA). COS-7 cells were plated onto two-chamber glass slides and transfected with 0.8- $\mu$ g DNA and 2- $\mu$ l FuGENE 6 reagent (Boehringer Mannheim, Indianapolis, IN). After 40 hours, cells were fixed in 3% paraformaldehyde, washed in phosphate-buffered saline (PBS), and blocked with 10% goat serum (Jackson Immunoresearch, West Grove, PA) and 5% fetal bovine serum (FBS) (Hyclone, Logan, UT) in PBS, with or without 0.1% Triton X-100. Blocked cells were incubated with rabbit antibody to mouse ANK primary antibodies diluted 1:50 (Ab1), 1:200 (Ab2), or 1:500 (Ab3) in blocking solution, incubated with fluorescein isothiocyanate (FITC)-conjugated Affinipure goat antibody to rabbit immunoglobulin G (IgG) secondary antibodies (Jackson Immunoresearch) diluted 1:143 in blocking solution, and washed in PBS. Nuclei were counterstained with 10  $\mu$ g/ml 7-AAD (Molecular Probes, Eugene, OR). Confocal images were captured on an MRC 1000 Confocal Imaging Microscope (Biorad, Richmond, CA).
20. Y. Gluzman, *Cell* **23**, 175 (1981).
21. A. M. Ho, M. D. Johnson, D. M. Kingsley, data not shown.
22. Other topologies are possible, including one in which the first hydrophobic stretch serves as a signal sequence instead of a transmembrane region.
23. Adult multiple tissue Northern blots were hybridized in ExpressHyb solution (Clontech, Palo Alto, CA) with a <sup>32</sup>P-labeled probe containing the complete *ank* ORF. Forelimbs from E16.0 mouse embryos were frozen, sectioned on a cryostat microtome, and hybridized with a 380 base pair (bp) digoxigenin-labeled cRNA probe from the 3' untranslated region (UTR) of *ank* as described [E. E. Storm and D. M. Kingsley, *Development* **122**, 3969 (1996)].
24. A. M. Ho, M. D. Johnson, D. M. Kingsley, unpublished data.
25. Detailed methods available on request.

26. Marker Hs. 11974 in P. Deloukas *et al.*, *Science* **282**, 744 (1999).
27. A. E. Hughes *et al.*, *Hum. Mol. Genet.* **4**, 1225 (1995).
28. L. J. Andrew *et al.*, *Am. J. Hum. Genet.* **64**, 136 (1999).
29. K. Rojas *et al.*, *Genomics* **62**, 177 (1999).
30. G. Lust, G. Faure, P. Netter, J. E. Seegmiller, *Science* **214**, 809 (1981).
31. Skin samples were removed from pairs of age- and sex-matched wild-type and *ank* mice, minced, and dissociated at 37°C in medium containing 0.05% trypsin, 0.53 mM EDTA, dispase (2.5 U/ml), and collagenase (200 U/ml). Attached skin fibroblasts were grown in Dulbecco's minimum essential medium (DMEM) containing 15% FBS, 2 mM GlutaMax, 0.1 mM nonessential amino acids, penicillin G (100 U/ml), streptomycin (100 µg/ml), and amphotericin B (0.25 µg/ml). Intracellular pyrophosphate levels were determined by coupled enzymatic and fluorimetric assay [G. Lust and J. E. Seegmiller, *Clin. Chim. Acta* **66**, 241 (1976)]. Extracellular pyrophosphate was determined by incubating cells in 3 ml of DMEM (10% FBS, 2 mM GlutaMax, 0.1 mM nonessential amino acids, no phenol red) for 48 hours. Conditioned medium (500 µl) was pre-cleared by centrifugation, adjusted to 1 M perchloric acid, and centrifuged. The supernatant was neutralized with 4 M KOH, centrifuged to remove KClO<sub>4</sub> precipitate, and assayed for pyrophosphate as above. Sample means were compared with the use of the Student's *t* test.
32. H. Fleisch, *Metab. Bone Dis. Relat. Res.* **3**, 279 (1981).
33. \_\_\_\_\_ and S. Bisaz, *Nature* **195**, 911 (1962).
34. Primary mouse fibroblasts ( $0.5 \times 10^6$  to  $1 \times 10^6$ ) or simian COS-7 cells ( $1 \times 10^6$  to  $2 \times 10^6$ ) were plated in 100-mm dishes, grown for 6 to 12 hours, and incubated for 4 to 6 hours in serum-free medium with DNA (5 µg), Plus reagent (18 µl), and Lipofectamine (18 µl)(Gibco-BRL). Following transfection, cells were grown in fresh antibiotic-free medium for 36 to 48 hours before assay. Control experiments with a pCMV-lacZ plasmid showed about fivefold higher expression levels in COS-7 cells than in mouse fibroblasts under these conditions.
35. S. E. Guggino, G. J. Martin, P. S. Aronson, *Am. J. Physiol.* **244**, F612 (1983).
36. A. K. Rosenthal and L. M. Ryan, *J. Rheumatol.* **21**, 896 (1994).
37. H. Fleisch, D. Schibler, J. Maerki, I. Frossard, *Nature* **207**, 1300 (1965).
38. H. Fleisch *et al.*, *Am. J. Physiol.* **211**, 821 (1966).
39. A. M. Caswell, M. P. Whyte, R. G. Russell, *Crit. Rev. Clin. Lab. Sci.* **28**, 175 (1991).
40. A. Okawa *et al.*, *Nature Genet.* **19**, 271 (1998).
41. I. Nakamura *et al.*, *Hum. Genet.* **104**, 492 (1999).
42. D. J. White *et al.*, *J. Clin. Dent.* **7**, 46 (1996).
43. W. P. Tew *et al.*, *Biochemistry* **19**, 1983 (1980).
44. H. E. Krug *et al.*, *Arthritis Rheum.* **36**, 1603 (1993).
45. P. Dieppe and I. Watt, *Clinics Rheum. Dis.* **11**, 367 (1985).
46. D. T. Felson *et al.*, *J. Rheumatol.* **16**, 1241 (1989).
47. P. A. Gibilisco, H. R. Schumacher, Jr., J. L. Hollander, K. A. Soper, *Arthritis Rheum.* **28**, 511 (1985).
48. A. Swan *et al.*, *Ann. Rheum. Dis.* **53**, 467 (1994).
49. M. Doherty, I. Watt, P. A. Dieppe, *Lancet* **i**, 1207 (1982).
50. A. L. Concoff and K. C. Kalunian, *Curr. Opin. Rheumatol.* **11**, 436 (1999).
51. L. M. Ryan and H. S. Cheung, *Rheum. Dis. Clin. North Am.* **25**, 257 (1999).
52. We thank M. Wagener for excellent assistance with animal experiments and G. Barsh and members of the Kingsley lab for helpful comments on the manuscript. A.M.H. is a trainee of the Medical Scientist Training Program at Stanford, supported by NIH training grant 5T32GM07365 (NIGMS). The initial stages of the genetic cross were supported by a Stanford-SmithKline Beecham research award. D.M.K. is an HHMI assistant investigator.

18 April 2000; accepted 6 June 2000

## Causes of Climate Change Over the Past 1000 Years

Thomas J. Crowley

Recent reconstructions of Northern Hemisphere temperatures and climate forcing over the past 1000 years allow the warming of the 20th century to be placed within a historical context and various mechanisms of climate change to be tested. Comparisons of observations with simulations from an energy balance climate model indicate that as much as 41 to 64% of preanthropogenic (pre-1850) decadal-scale temperature variations was due to changes in solar irradiance and volcanism. Removal of the forced response from reconstructed temperature time series yields residuals that show similar variability to those of control runs of coupled models, thereby lending support to the models' value as estimates of low-frequency variability in the climate system. Removal of all forcing except greenhouse gases from the ~1000-year time series results in a residual with a very large late-20th-century warming that closely agrees with the response predicted from greenhouse gas forcing. The combination of a unique level of temperature increase in the late 20th century and improved constraints on the role of natural variability provides further evidence that the greenhouse effect has already established itself above the level of natural variability in the climate system. A 21st-century global warming projection far exceeds the natural variability of the past 1000 years and is greater than the best estimate of global temperature change for the last interglacial.

The origin of the late-20th-century increase in global temperatures has prompted considerable discussion. Detailed comparisons of climate model results with observations (1) suggest that anthropogenic changes, particularly greenhouse gas (GHG) increases, are probably responsible for this climate change. However, there are a number of persistent questions with respect to these conclusions that involve uncertainties in the level of low-frequency unforced variability in the climate system (2) and whether factors such as an

increase in solar irradiance or a reduction in volcanism might account for a substantial amount of the observed 20th-century warming (1, 3–10). Although many studies have addressed this issue from the paleoclimate perspective of the past few centuries (3–10), robust conclusions have been hampered by inadequate lengths of the time series being evaluated. Here I show that the agreement between model results and observations for the past 1000 years is sufficiently compelling to allow one to conclude that natural variability plays only a subsidiary role in the 20th-century warming and that the most parsimonious explanation for most of the warming is that it is due to the anthropogenic increase in GHG.

### Data

The data used in this study include physically based reconstructions of Northern Hemisphere temperatures and indices of volcanism, solar variability, and changes in GHGs and tropospheric aerosols.

*Northern Hemisphere temperatures.* Four indices of millennial Northern Hemisphere temperature have been produced over the past 3 years (11–14). The analysis here uses the mean annual temperature reconstructions of Mann *et al.* (11) and of Crowley and Lowery (CL) (12), because the energy balance model used in this study calculates only this term [the other records (13, 14) are estimates of warm-season temperature at mid-high latitudes]. The Mann *et al.* reconstruction was determined (8) by first regressing an empirical orthogonal function analysis of 20th-century mean annual temperatures against various proxy indices (such as tree rings, corals, and ice cores). Past changes in temperature are estimated from variations in the proxy data (15). The Mann *et al.* reconstruction has a varying number of records per unit of time (although the number in the earlier part of the record is still greater than in CL). The CL reconstruction is a more heterogeneous mix of data than the Mann *et al.* reconstruction, but the number of records is nearly constant in time. It is a simple composite of Northern Hemisphere climate records and was scaled (12) to temperature using the instrumental record (16) in the overlap interval 1860–1965. The instrumental record was substituted for the proxy record after 1860 for two reasons: (i) there were too few proxy data in the CL time series after 1965 to reconstruct temperatures for this interval, and (ii) the original CL reconstruction indicated a “warming” over the interval 1885–1925 that is at variance with the instrumental record. This difference has been attributed (11, 17) to

Department of Oceanography, Texas A&M University, College Station, TX 77843, USA. E-mail: tcrowley@ocean.tamu.edu